

Journal of Materials Chemistry C

Accepted Manuscript



This is an *Accepted Manuscript*, which has been through the Royal Society of Chemistry peer review process and has been accepted for publication.

Accepted Manuscripts are published online shortly after acceptance, before technical editing, formatting and proof reading. Using this free service, authors can make their results available to the community, in citable form, before we publish the edited article. We will replace this *Accepted Manuscript* with the edited and formatted *Advance Article* as soon as it is available.

You can find more information about *Accepted Manuscripts* in the [Information for Authors](#).

Please note that technical editing may introduce minor changes to the text and/or graphics, which may alter content. The journal's standard [Terms & Conditions](#) and the [Ethical guidelines](#) still apply. In no event shall the Royal Society of Chemistry be held responsible for any errors or omissions in this *Accepted Manuscript* or any consequences arising from the use of any information it contains.

Red to near infrared ultralong lasting luminescence from Mn²⁺-doped sodium gallium aluminum germanate glasses and (Al,Ga)-albite glass-ceramics

Pengfei Li,^a Mingying Peng,^{a*} Lothar Wondraczek,^b Yanqi Zhao,^a Bruno Viana,^c

^a The China-Germany Research Center for Photonic Materials and Devices, The State Key Laboratory of Luminescent Materials and Devices, School of Materials Science and Engineering, South China University of Technology, Guangzhou 510641, China

^b Otto Schott Institute of Materials Research, University of Jena, 07743 Jena, Germany

^c IRCP Chimie ParisTech, 11 rue Pierre et Marie Curie, 75231 Paris Cedex 05, France

*pengmingying@scut.edu.cn

Abstract

For specific techniques of either bioimaging or tumor photodynamic therapies, it is crucial to find an optical material with emission wavelengths desirable in the tissue transparent region of 650 to 1300nm and luminescence persistence longer than hours. We show here first a new red to near infrared persistent luminescence from Mn²⁺ doped sodium gallium aluminum germanate glasses which covers the 600nm to 800nm. The octahedral Mn²⁺ persistent luminescence correlates tightly to the electron filled defects with depths of 0.71eV, 0.80eV and 1.06eV, respectively, which can be detrapped thermally at room temperature. The detrapping can persist longer than 40 hours. When nanocrystalline high-albite Na(Al,Ga)Ge₃O₈ is precipitated from the supercooled melt through controlled thermal annealing, the red afterglow can be preserved, and the duration can be notably extended to longer than 100 hours. This originates from the incorporation of Mn²⁺ on octahedral sites with a more ionic bonding character in the compound, and the significant increase of density of defects which depths decrease to 0.70eV, 0.75eV and 0.85eV, respectively. The improved performance from tens of nanometer sized Na(Al,Ga)Ge₃O₈ implies their potential in *in-vivo* bioimaging or tumor photodynamic therapies after further optimization, such as shaping and grafting of functional surface layers in future.

1. Introduction

Afterglow luminescence, i.e., luminescence which persists when the external illumination source has been removed, has been known for several centuries. This phenomenon has found wide-ranging applications, e.g., for emergency escape route and exit signs, indoor and outdoor decoration or toys, optical data storage, lighting, temperature sensors or sensors for detecting structural failure.¹⁻⁵ The versatility of materials with useful phosphorescence properties, however, and, in particular, the availability of various emission colors has been surprisingly limited until the last two decades, when, besides the above mentioned applications, new fields of interest emerged in biomedical sensing and imaging. Chen *et al.*⁶ demonstrated X-ray induced persistent luminescent nanoparticles for photodynamic treatment of cancer. They grafted the nanoparticles with photosensitizers which could be excited *in situ* by the afterglow light released from nanoparticles.⁶ The excited photosensitizer can subsequently transform triplet oxygen into the

singlet state, what has been considered as a way to kill tumor cells. The overall idea was to enable a more localized tumor treatment and, hence, reduce the need for invasive treatment. Le Masne De Chermont *et al*⁷ reported on the use of persistent luminescence as fluorescent probe for *in vivo* tumor imaging. This was enabled by an afterglow duration of more than one hour after removing the excitation source. Then, the luminescent probe does not need to be excited with external light sources during imaging which avoids signal interference with the autofluorescence of the analyzed tissue. It was demonstrated that notable improvements in image quality and signal-to-noise-ratio can be obtained in that way. These two promising applications have soon turned persistent luminescence materials into very hot research topics in following years.⁸⁻¹³

The two essential applications necessitate the persistent luminescence materials with suitable emission wavelengths and afterglow time. The emission should better occur in the transparency window of biological tissue, i.e., in the spectral range of ~650-1300 nm. The afterglow time should better be longer than a few hours. It is the aim of our work to find such candidate materials.

This actually has stimulated the searches on the promising materials, and it has led to the series of findings. These include rare earth (RE) or transition metal (TM) doped persistent phosphors.¹²⁻²³ For RE-based phosphors, latest advances are on Eu²⁺-doped nitrides and Eu³⁺-doped tungstates, e.g., M₂Si₅N₈:Eu²⁺ or MWO₄:Eu³⁺.^{22,23} Their emission, however, peaks at wavelengths below 650 nm, and the afterglow time is typically less than one hour.²³ So far as we know, the most promising phosphors are trivalent chromium doped gallates.^{4, 11, 12, 21} Pan *et al*⁴ reported an afterglow duration longer than 360 h as Zn and Ge were substituted for Ga sites. In those materials, luminescence covers the spectral range of 680 to 750 nm, due to the Cr³⁺ transition ²E→⁴A₂ in the octahedral surroundings.

For TM-based persistent phosphors, there are also reports on Mn²⁺ doped persistent phosphors but mainly centering on silicate, germanate or phosphates.^{9, 21, 26, 27} The luminescence mostly occurs over the spectral range of 600 to 750nm, and it comes from the octahedral sites of Mn²⁺ (^VMn²⁺) once doped into the crystalline phase.²⁸ Mn²⁺ doped glasses were also reported with red emissions with lifetime in the millisecond regime such as zinc borosilicates and germanates.^{29-31,32-34} As the glass samples were devitrified, it has been found that Mn²⁺ emission will become into green emission^{32-34,35} This is because usually tetrahedral cation sites are predominant in the crystals precipitated inside glass, and Mn²⁺ ions will be driven into the tetrahedral lattice sites in weak crystal field during crystallization process. So far, the afterglow of ^VMn²⁺-related red photoemission is seldom longer than one hour either in crystals, glasses or glass ceramics. There are also very few report on glass ceramics which can stabilize ^VMn²⁺ emission centers in crystalline rather than glass phase. Is it possible inside a glass to precipitate a crystalline phase which comprises octahedral host cationic sites Mn²⁺ ions prefer to reside? If so, will the Mn²⁺ luminescent afterglow be longer than one hour?

In this work, we select germanate glass as target host because Mn²⁺ red afterglow has been found in the glass system and the glowing duration has not been mentioned yet.^{33,34,35-37} We are

looking for a glass and glass ceramic system in which, upon devitrification, Mn^{2+} will remain in octahedral coordination, but will at least partially be incorporated into the crystal phase (rather than being accumulate in the residual glass phase). We select Mn^{2+} as the activator ions rather than Cr^{3+} . This is partially because Mn^{2+} can show similar red to near infrared emission to Cr^{3+} , and partially because Cr^{3+} containing materials once exposed to oxygen rich environments will tend to be oxidized perhaps into higher valence states such as Cr^{6+} . This species is highly toxic and easily leads to cancer once mistaken into human body. Since Cr^{3+} exhibits the outstanding persistent luminescence in gallate, we introduced gallium on purpose into the germanate glass and wish it could help improving Mn^{2+} afterglow properties.^{4, 13, 21, 38} Besides, we added percentage of glass modifier ions Na^+ , which can breakdown the germanate glass network and therefore lower the melting temperature.

We show in the following that Mn^{2+} -doped sodium gallium germanate glass indeed exhibit red persistence luminescence in the spectral range of 600nm to 800nm and afterglow can persist longer than 48 hours at a dopant content of 0.1% Mn^{2+} . Out of our expectation is that nanocrystalline $\text{Na}(\text{Ga},\text{Al})\text{Ge}_3\text{O}_8$ phase can be precipitated from the supercooled melt and it comprises the sodium octahedral sites and the aluminum/germanium/gallium sites. Mn^{2+} doped glass ceramics can preserve the red emission of Mn^{2+} ions which substitute for sodium sites in $\text{Na}(\text{Ga},\text{Al})\text{Ge}_3\text{O}_8$ (see Fig. 1), and in the meanwhile, the emission intensity can be enhanced while the persistence of luminescence can be improved longer than 100h. We have employed different techniques such as static and dynamic excitation and photoluminescence spectra, electron paramagnetic resonance spectrum, thermoluminescence, time resolved emission spectrum, and high resolution transmission electron microscopy *etc* to unravel how the red persistent luminescence of Mn^{2+} comes into being and why it can be significantly improved in glass ceramics samples, and evaluate whether it can find application in tumor bioimaging or photodynamic therapy.

2. Experimental

2.1. Syntheses

All glass samples were produced through conventional melting at high temperature and subsequent quenching. For this, analytical grade reagents Na_2CO_3 and MnCO_3 , and high pure GeO_2 (5N) and Ga_2O_3 (4N) were used as the starting materials. Batches of 20 g were weighed accurately according to the molar composition $8\text{Na}_2\text{O}-12\text{Ga}_2\text{O}_3-80\text{GeO}_2$. MnCO_3 was added for Mn^{2+} -doping in nominal quantities of 0-3.0 mol%. The batches were thoroughly mixed and filled into alumina crucibles. Each batch was then melted in a resistively heated furnace at 1550 °C for 30 min under ambient atmosphere. The melts were poured onto a preheated stainless steel plate and splash-cooled by pressing with another stainless steel stamp. The solidified samples were subsequently annealed at 350 °C for 10 h. Thus obtained visually transparent and colorless glass samples were cut into a size of 10mm×10mm×1mm and polished for the following optical analyses and heat treatment procedures. For referencing, labels G-Mn-x are used, where x stands

for the nominal amount of added Mn^{2+} in mol%. Differential scanning calorimetry was used to determine the peak temperature of crystallization, $T_c = 695$ °C for G-Mn-0.1. Crystallization treatments of this latter sample were performed at this temperature for holding times of 0.5 h, 1 h, 2 h and 5 h. In the following, these samples are labelled GC-0.5h, GC-1h, GC-2h and GC-5h, respectively.

2.2. Characterization

Static excitation and emission spectra, emission lifetime data and dynamic emission decay spectra were recorded on a high resolution spectrofluorometer (Edinburgh Instruments FLS 920), equipped with a red-sensitive single photon counting photomultiplier (Hamamatsu R928P) in a Peltier air-cooled housing over the spectral range of 200 to 900 nm. A pulsed xenon flash lamp (pulse duration \sim ms, $\mu\text{F}900$) with an average power of 60 W, and a 450 W xenon lamp were used as excitation sources, respectively, for the emission decay curves and the steady-state measurements. Absorption spectra were measured with a UV/VIS/NIR spectrophotometer (Lambda-900, PerkinElmer, USA). Differential scanning calorimetry (DSC) was performed with a STA449C Jupiter (Netzsch, Germany) in ambient atmosphere at a heating rate of 10 K/min in the range from 20 to 1200 °C. X-ray diffraction (XRD) patterns of the glass-ceramics were recorded with a Rigaku D/max-III A X-ray diffractometer (40 kV, $1.2^\circ \text{ min}^{-1}$, 40 mA, $\text{Cu-K}_{\alpha 1}$, $\lambda = 1.5405$ Å). The crystal morphology and size distribution were analyzed with a high-resolution transmission electron microscope (HRTEM, 2100F, JEOL, Japan), equipped with an energy-dispersive spectrometer (EDS) system to map the chemical elements distribution. Electron paramagnetic resonance (EPR) spectra were recorded at 85 K with an X-band spectrometer (Bruker A300).

The afterglow decay curves and thermoluminescence (TL) curves were measured with a FJ427A1 thermoluminescent dosimeter (CNNC Beijing Nuclear Instrument Factory). Before each measurement, the samples were first heated to 250 °C to completely de-trap all electrons and to heal-out eventual pre-existing (shallow) defects. An amount of 0.005 g of powder was weighed for each sample and exposed to 254nm illumination from a mercury lamp at an output power of 60 W for 5 min. Subsequently, with a total delay time of 30 s after removal of the excitation source, photoluminescence decay curves were recorded. After a total delay of 10 min, TL curves were recorded. The range of the TL curves measurement was from room temperature (RT) to 250 °C with a scanning rate of 1 °C \cdot s $^{-1}$. If not otherwise stated, all other measurements were performed at room temperature.

3. Results and discussion

3.1. Photoluminescence from $^{55}\text{Mn}^{2+}$ doped germanate glass

All the Mn^{2+} -doped or undoped germanate glasses are visually colorless and transparent. When exposed to 254nm irradiation, red photoemission is readily visible in all Mn^{2+} -doped samples, whereas the undoped samples do not exhibit red PL. The red PL is therefore clearly assigned to the presence of manganese. Exemplary EPR spectra of glassy and glass ceramic samples are shown in

Fig. 2. The typical sextet structure with a resonance at $g = 1.9941$ is associated with magnetic dipolar transitions of Mn^{2+} in a highly symmetric state.³⁹ The hyperfine splitting which is observed in G-Mn-0.1 is indicative for isolated Mn^{2+} ions, similar to observations on other glasses.^{28, 40} In the glass ceramic samples GC-1h and GC-5h, the sextet is less clearly visible. While it is not fully quenched-out, this points to weak Mn^{2+} - Mn^{2+} magnetic interactions. We see a sharpening of the main resonance, now at $g = 1.9933$, with progressing time of crystallization treatment, but the width and constriction of the signal remain practically unchanged during crystallization. The latter indicates that there is no increase in the magnetic interactions between Mn^{2+} ions during crystallization, what would have resulted in exchange narrowing of the signal.²⁸ This is an important observation as it indicates that during crystallization, there is no notable agglomeration of Mn^{2+} species in the residual glass phase and, hence, that Mn^{2+} is incorporated into the crystalline phase. The EPR linewidth of the main signal is about 40 mT for all samples, which is rather low and indicates the presence of edge-sharing VI^{2+} polyhedra. As will be discussed later, this is in good agreement with the crystallographic analyses which evidence the presence of triclinic high-albite, $\text{Na}(\text{Al,Ga})\text{Ge}_3\text{O}_8$, in which Mn^{2+} may be incorporated on the octahedral sites edge-shared with the tetrahedral sites. The slight but significant down-shift in the g -value reflects a change in bond character to more ionic bonding.

Photoluminescence spectra of all samples are shown in Fig. 3a. Upon excitation at 250 nm, all doped glasses show a pronounced, broad emission band spanning the spectral range of 550 nm to 800 nm, originating from the spin-forbidden ${}^4\text{T}_1({}^4\text{G}) \rightarrow {}^6\text{A}_1({}^6\text{S})$ transition in VI^{2+} .^{30-32, 41-44} With increasing manganese content, the emission peak red-shifts gradually (Fig. 3a-b). At the same time, the emission intensity increases up to $x=2.0$, and decreases for higher x , apparently due to concentration quenching. The PL decay curve follows well a single exponential function for as long as $x \leq 0.5$. At higher x , a multi-exponential function is required to fit the experimental decay data, indicating that at least two different emission species are active in these cases (Fig. 3c).

For a persistent luminescent material, the luminescence persistence is contributed by the activator lifetime, and the detrapping time which corresponds to the time when electrons are thermally discharged from the defect centers and then transferred to the activator, here Mn^{2+} . To qualitatively understand how the PL lifetime changes with Mn^{2+} content, we define the PL lifetime as the time when the PL intensity decreases to the e^{-1} fold of the initial intensity. This was produced by fitting each curve to a single exponential equation and depicted as inset of Fig. 3c. It is in the order of milliseconds for all samples and it implies the effect of concentration quenching. To reveal the mechanism which dominates the quenching effect, we fitted the concentration dependence of emission intensity to the classic equation:⁴⁵

$$I = x \times [k / (1 + \beta \times (x/x_c')^{\theta/3})] \quad (1)$$

, where I is the integrated emission intensity at concentration x ; x_c' is the critical concentration; k and β are constants for specific interaction in the host; and $\theta = 6, 8, 10$ stand for electric dipole-dipole, dipole-quadrupole, and quadrupole-quadrupole interactions, respectively. The

fitting correlation coefficient is 92.97%, 87.61% and 81.87% for $\theta = 6, 8, 10$, respectively (see Fig.3b). This means the electric dipole-dipole interaction is dominating the quenching process.

PL excitation spectra are shown in Fig. 3d. For all Mn^{2+} -doped samples, they comprise a dominant band at ~ 250 nm with a broad shoulder from 275 nm to 375 nm, and a well-separated sharp peak at ~ 413 nm with another shoulder at approximately 500 nm. The corresponding band assignments are given in Fig. 3d.²⁹⁻³¹ Also the excitation peaks exhibit a red-shift with increasing Mn^{2+} content. Obviously, the shoulder band peaking at about 500 nm extends to >550 nm. It therefore overlaps with the emission spectrum, meaning that re-absorption may occur especially at higher content of Mn^{2+} (see Fig. 3a and 3d). This is taken as one of the reasons for the observed red-shift in the emission and excitation spectra. Noteworthy, there is another weak band occurring at around 410nm. We assign this to the presence of oxygen-defects on Ge^{4+} entities, Ge-associated oxygen defects (GODCs).^{34, 46} Similar defects have been observed in germanate glasses previously.^{31, 46} Their intensity decreases with increasing Mn^{2+} content due to energy transfer from GODCs to Mn^{2+} .

3.2. Persistent luminescence from Mn^{2+} doped germanate glass

Upon removal of the UV-C excitation source, all Mn^{2+} doped samples exhibit visible red afterglow. Fig. 4 shows exemplary photographs of this. Obviously, afterglow duration and intensity, respectively, strongly depends on dopant concentration and (as will be discussed in the following paragraphs) on the degree of crystallization. Afterglow decay spectra of sample G-Mn-0.1 are depicted in Fig. 5. Within the first 15 s of decay, the peak position of Mn^{2+} -related photoemission shifts from 643 nm to 670 nm. Some further but less pronounced red-shift, i.e., to 677 nm, is observed in the following 4 min. Subsequently, the peak position remains constant. This transition indicates a convolution of rapid and slow decay processes, assumedly originating from different emission centers which are present in the glass sample. The slow decay process can persist longer than 48hours (see Fig.5). In Fig. 6, we depict thermoluminescence (TL) spectra as a tool to assess the depth of the electronic traps which are the assumed origin for the persistence of PL. For sample G-Mn-0.1, the TL curve is dominated by a single broad band which covers the temperature range of 300 to 525 K. This generally reflects a wide energetic distribution of traps. An accurate fit of the experimental spectrum is obtained with an overlay of three Gaussian functions centered at 354, 401 and 529 K. We employ Urbach's method in order to quantify the depth of individual traps through fitting those peaks to the experimental data,^{47, 48} i.e., $E = T_m/500$, where E is the thermal activation energy or the depth of the trap level in eV, and T_m (K) is the peak temperature of the underlying Gaussian. Derived values are summarized in Table 1. For the glass G-Mn-0.1, we obtain at least three types of traps with depth of 0.71, 0.80 and 1.06eV, respectively.

3.3. Enhanced PL and persistent luminescence from $\text{V}^{1+}\text{Mn}^{2+}$ doped germanate glass ceramics

Thermal treatment of the glass specimen results in the precipitation of a nanocrystalline

secondary phase. The details of this process will be discussed in the subsequent paragraph. Here, we first consider its effect on the PL performance of the material, assuming that through crystal precipitation, the optically active $^{VI}Mn^{2+}$ species can be forced into an ordered octahedral ligand field with strongly enhanced PL afterglow duration. Since the sample G-Mn-0.1 already as a glass has the longest PL lifetime of all samples (Fig. 3c), we focus on this composition in the following experiments. As already noted, thermal treatment was performed on the basis of prior DSC analyses. After crystallization, the visual color of PL from the sample changes from deep red to orange, see Fig. 4. The corresponding PL spectra are shown in Fig. 7. With the onset of crystallization, there is a clear red-shift of the broad main emission peak, i.e., from ~ 643 nm to ~ 671 nm. At the same time, a weaker green emission band appears at ~ 530 nm, indicating re-precipitation of Mn^{2+} in a less-strong ligand field, i.e., tetrahedral $^{IV}Mn^{2+}$.³²⁻³⁴ The appearance of this band is the reason for the apparent change in PL color. Inset of Fig.7a shows the dependence of integrated emission intensity on the crystallization time. The integration was made over the spectral range from 350nm to 820nm. It depicts that the intensity of glass ceramic sample is stronger than the glass sample. We further notice that particularly for the sample GC-5h, the overall PL intensity is enhanced \sim two times over that of the glassy sample. Fig. 7b shows the excitation spectra of the glass ceramics samples, recorded for the $^{VI}Mn^{2+}$ species. The assignment of the excitation band is similar to G-Mn-0.1.

With the removal of the excitation source, all glass ceramics exhibit more intense and longer afterglow. This is especially the case for sample GC-5h (see Fig. 8). Noteworthy, even after 104h, some afterglow could still be detected. Fig. 9 shows the time resolved emission spectra of GC-5h, which were measured at different delay times from 15 seconds to 104hours. A strong blue-shift of the emission peak occurs within the first 15s, i.e., from 671 nm to 635 nm (see Fig. 9 and 7a). Subsequently, the peak slightly red-shifts to ~ 650 nm (see the 30h to 104h delayed curves in Fig.9). This implies multiple $^{VI}Mn^{2+}$ emission centers in the glass ceramic sample. The green PL band which was attributed to $^{IV}Mn^{2+}$ does not show persistent luminescence after removal of the excitation source (see Fig. 9).

TL, XRD and EPR spectra of glass ceramic samples were collected to understand the observed differences between glass and glass ceramic samples. The TL spectra indicate that the strongest peak occurs at ~ 360 K in the glass ceramic, at a lower temperature than in the glassy specimen (see Fig. 6). This means that the energetic depth of the underlying defect is slightly lower. Again, we obtain an accurate fit with three Gaussian bands (Table 1). For GC-5h, the corresponding defect depths are 0.70eV, 0.75eV and 0.85eV, respectively, all lower than the ones observed in G-Mn-0.1. This might be due to the substitution of gallium ion with a higher ionization energy (IE) 2963KJ/mol for aluminum ion (IE=2745KJ/mol) in glass ceramic samples as will be discussed below. The decrease of the content of codopant with lower IE will make the traps shallower. This was observed similarly in $ZnS:Cu^+,Co^{2+}$.¹⁴ The much higher intensity of TL emission further indicates a much higher number density of those defects.

Fig. 10 shows the XRD pattern of the glass samples G-Mn-0.1 after different crystallization times (0~5h). As expected, there are no obvious diffraction peaks in the glass sample, nor in the sample GC-0.5h. This indicates that those two samples are amorphous, or that the crystals are too small to cause lattice diffraction. For GC-0.5h, we expect the latter because we did observe the green emission band in the PL spectra which we took as evidence for the occurrence of some $^{IV}\text{Mn}^{2+}$. In GC-1h, GC-2h and GC-5h, sharp diffraction peaks appear and grow further with prolonged treatment time. We use Scherrer's equation to obtain a rough estimate of the corresponding crystallite size, $D=K\lambda/\beta\cos\theta$, where D is the crystallite size, K is a dimensionless shape factor, λ is the X-ray wavelength, β (rad) is the line broadening at half maximum (FWHM), and θ (rad) is the Bragg angle. The strongest diffraction peak with $2\theta=27.02^\circ$ was selected for the calculation, yielding an average size of ~30 nm, 50 nm and 60 nm for GC-1h, GC-2h and GC-5h, respectively. For GC-5h, the morphology and size distribution of those nanocrystals was also analyzed by HR-TEM, see Fig. 11a, where irregular crystallites with a size ~20-50 nm were observed. The lattice fringes can be observed in higher resolution image as inset of Fig. 11a shows, and the distance between neighbored crystal lattice fringes is ~0.328nm, and it corresponds to the (002) crystal facet of albite $\text{Na}(\text{Al,Ga})\text{Ge}_3\text{O}_8$. This consists with the diffraction patterns of Fig. 10, which point to a triclinic phase of space group $\bar{C}1$, $\text{NaAlGe}_3\text{O}_8$ (ICSD #61170). Ga^{3+} can readily substitute for Al^{3+} to form the gallium albite, $\text{Na}(\text{Al,Ga})\text{Ge}_3\text{O}_8$, which we expect to occur in the present case. We relate the presence of Al^{3+} to crucible dissolution, what was confirmed by two-dimensional element mapping analysis as shown in Fig. 11b-f. Sodium, germanium, aluminum, gallium and oxygen are homogeneously distributed throughout the sample.

The Rietveld refining was made with FullProf Suite Program version 2011, and it starts with the crystallographic data of $\text{NaAlGe}_3\text{O}_8$ (ICSD #61170). The refining produces lattice parameters of $a=8.4063\text{\AA}$, $b=13.2844\text{\AA}$, $c=7.3389\text{\AA}$, $\alpha=94.39$, $\beta=116.28$, $\gamma=90.86$ and $V=731.59\text{\AA}^3$ for sample GC-5h. The cell volume is a little bigger than 731.47\AA^3 (ICSD #61170). This expansion of the cell is a sign for the incorporation of gallium into the $\text{NaAlGe}_3\text{O}_8$ compound and, thus, for the formation of the solid solution $\text{Na}(\text{Al,Ga})\text{Ge}_3\text{O}_8$. It is also consistent with the shifts of the diffraction peaks to somewhat lower angles as compared to the pure high-albite (see Fig. 10). High-albite comprises one type of octahedral sodium sites and four types of tetrahedral Ge/Al/Ga sites. When manganese ions are introduced, considering their radius alone, they can assumedly substitute for either sodium or for any of the tetrahedral sites. The latter explains the occurrence of some green PL, while the former is taken to be at the origin of prolonged afterglow.

3.4. Afterglow mechanism

Inspecting more carefully the PL and the afterglow spectra of the Mn^{2+} doped glass ceramics (see Fig. 7a and Fig. 9), we find notable differences, especially in the green spectral range. The green emission is absent from the afterglow spectra. This implies that the persistent luminescence mechanism is not due to a process which involves thermally activated electrons released from

traps and consequently tunneling through conduction band. The latter would be the case if trapped electrons are thermally emitted from the traps and lifted to the conduction band. Subsequently, they can be captured by the activator ions. Afterglow is then a result of the recombination of electrons and holes. If this route dominated the emission process, also the green emission of ${}^{\text{IV}}\text{Mn}^{2+}$ should be visible in the afterglow since the higher-lying excited level from which this emission occurs is much closer to the conduction band as compared to the gap between the red-emitting level and the conduction band. On this basis, we propose the mechanism, as schematically shown in Fig. 12.

When the samples were illuminated with ultraviolet light, different types of Mn^{2+} emission centers (named EC1, EC2 and EC3 but the number is for sake of visualization in Fig. 11) in the hosts are excited along path 1 into the ${}^4\text{T}_1$ (${}^4\text{P}$) state, the latter lying in the conduction band. This leads to a separation of electrons and holes. Holes subsequently follow path 2 and flow into the valence band. Simultaneous remove of electron and hole will not lead to the valence variation of manganese ion. Some electrons, on the other side, relax to the lower end of the conduction band via path 3. Another portion of electrons transits through the non-radiative path 4 to the different types of the shallow defects such as D1, D2 and D3. D1-D3 have the depths as summarized in Table 1. When the excitation source is removed, electrons start to escape the traps D1-D3 via path 5. Path 5 is thermally activated and it, hence, is slow at room temperature. The electrons can also be removed from D1 (or D2, D3) directly, and be trapped on the excited states of EC1 (or EC2, EC3). They can further also escape from a deeper defect to a shallower defect reversibly, and then be captured by the activators. In the meanwhile, thermal stimulation will lift holes from valence band to the ground state via path 2. Once the electrons are trapped on EC1 (EC2, EC3), they emit their potential energy in the form of red light by recombining to holes. The relaxation dynamics, in turn, depend on the depth and the density of defects D1 to D3. As the Mn^{2+} doped glass is transformed into the glass ceramic, the defects become shallower and more populated. We did try to charge these shallow defects with other light sources such as 365 nm or 410 nm LEDs, but failed. This confirms that path 1 is the crucial process for lifting the electrons into the conduction band directly. Once electrons are in conduction band, they can move freely and, especially, charge the defects. The defects, as discussed in ref.14, may not be randomly distributed throughout sample. They with depth as presented Table 1 prefer gathering in vicinity of manganese sites. It, therefore, enables energy transfer possible from the defects to the activators.

In view of the ultralong lasting afterglow, we had tried to synthesize Mn^{2+} doped $\text{NaAlGe}_3\text{O}_8$ crystal by traditional high temperature solid state reaction but failed. Further works are obviously necessary on how to prepare the high pressure phase with controlled size and morphology by other techniques rather than currently crystallization from glass phase. Usually for nanosized persistent luminescence materials, the persistence will be greatly shortened especially as compared to bulk materials. This work, however, shows the different, that the persistence can be preserved longer than 100h even when the doped crystalline phase of $\text{Na}(\text{Al,Ga})\text{Ge}_3\text{O}_8$ becomes as small as 50 nm.

This, plus luminescence in 600nm to 800nm range lying in the tissue transparent region, demonstrates its potential application in tumor bioimaging or photodynamic therapy. This study is the first and primary step towards it.

4. Conclusions

In this work, we found a new type of Mn^{2+} doped sodium gallium aluminum germanate glass which can exhibit red to near infrared luminescence persisting longer than 48h in the spectral range from 600 to 800nm. The persistence of Mn^{2+} red luminescence can be preserved and improved even longer than 100h through controlled crystallization and defect engineering (modulation of defect depth and density as Fig. 6 and Table 1 reveal). This is thanks to successfully inducing in glass the formation of albite $\text{Na}(\text{Al,Ga})\text{Ge}_3\text{O}_8$ which comprises sodium octahedral sites, and therefore, stabilizes the red emissive Mn^{2+} ions. The controlled crystallization can lead to the precipitated crystal $\text{Na}(\text{Al,Ga})\text{Ge}_3\text{O}_8$ with a size smaller than 50nm (see Figs. 10 and 11), and this small size of the nanocrystal does not quench the persistent luminescence as many reports have reported, and it, therefore, shows us new insights in the field of biomedical imaging or photodynamic therapy after further optimization and grafting of functional surface layers to the Mn^{2+} doped nanocrystals in the future.

Acknowledgements

The authors would like to acknowledge financial support from the National Natural Science Foundation of China (Grant No. 51322208 and 51132004), Guangdong Natural Science Foundation for Distinguished Young Scholars (Grant No. S20120011380), and the Department of Education of Guangdong Province (Grant No. 2013gjhz0001).

References

- 1 M. Peng, J. Qiu and Q. Zhang, *Opt. Mater.*, 2014, **36**, 1769-1770.
- 2 P. F. Smet, D. Poelman and M. P. Hehlen, *Opt. Mater. Express*, 2012, **2**, 452-454.
- 3 H. F. Brito, J. Hölsä, T. Laamanen, M. Lastusaari, M. Malkamäki and L. C. Rodrigues, *Opt. Mater. Express*, 2012, **2**, 371-381.
- 4 Z. Pan, Y.-Y. Lu and F. Liu, *Nat. Mater.*, 2012, **11**, 58-63.
- 5 H. Lin, B. Wang, J. Xu, R. Zhang, H. Chen, Y. Yu, Y. Wang, *ACS Appl. Mater. Interfaces*, 2014, **6**, 21264-21269.
- 6 W. Chen and J. Zhang, *J. Nanosci. Nanotechnol.*, 2006, **6**, 1159-1166.
- 7 Q. Le Masme de Chermont, C. Chanéac, J. Seguin, F. Pellé, S. Maîtrejean, J.-P. Jolivet, D. Gourier, M. Bessodes and D. Scherman, *Proc. Natl. Acad. Sci. U.S.A.*, 2007, **104**, 9266-9271.
- 8 K.-L. Wong, G.-L. Law, M. B. Murphy, P. A. Tanner, W.-T. Wong, P. K.-S. Lam and M. H.-W. Lam, *Inorg. Chem.*, 2008, **47**, 5190-5196.
- 9 T. Maldiney, A. Lecointre, B. Viana, A. I. Bessière, M. Bessodes, D. Gourier, C. Richard and D. Scherman, *J. Am. Chem. Soc.*, 2011, **133**, 11810-11815.
- 10 A. Abdukayum, J.-T. Chen, Q. Zhao and X.-P. Yan, *J. Am. Chem. Soc.*, 2013, **135**, 14125-14133.
- 11 T. Maldiney, A. Bessière, J. Seguin, E. Teston, S. K. Sharma, B. Viana, A. J. Bos, P. Dorenbos, M. Bessodes and D. Gourier, *Nat. Mater.*, 2014, **13**, 418-426.

- 12 S. Sharma, D. Gourier, B. Viana, T. Maldiney, E. Teston, D. Scherman and C. Richard, *Opt. Mater.*, 2014, **36**, 1901-1906.
- 13 Y. Li, S. Zhou, G. Dong, M. Peng, L. Wondraczek and J. Qiu, *Sci. Rep.*, 2014, **4**.
- 14 F. Clabau, X. Rocquefelte, T. Le Mercier, P. Deniard, S. Jobic and M.-H. Whangbo, *Chem. Mater.*, 2006, **18**, 3212-3220.
- 15 D. Chen, Y. Chen, H. Lu and Z. Ji, *Inorg. Chem.*, 2014, **53**, 8638-8645.
- 16 D. Kulesza, A. Wiatrowska, J. Trojan-Piegza, T. Felbeck, R. Geduhn, P. Motzek, E. Zych and U. Kynast, *J. Lumin.*, 2013, **133**, 51-56.
- 17 D. Kulesza and E. Zych, *J. Phys. Chem. C*, 2013, **117**, 26921-26928.
- 18 P. A. Tanner, in *Lanthanide Luminescence*, Springer, 2011, pp. 183-233.
- 19 J. Xu, Z. Ju, X. Gao, Y. An, X. Tang and W. Liu, *Inorg. Chem.*, 2013, **52**, 13875-13881.
- 20 S. Ye, J. Zhang, X. Zhang, S. Lu, X. Ren and X.-j. Wang, *J. Appl. Phys.*, 2007, **101**, 063545-063545-063546.
- 21 Y. Zhuang, Y. Katayama, J. Ueda and S. Tanabe, *Opt. Mater.*, 2014, **36**, 1907-1912.
- 22 F. Kang, Y. Hu, L. Chen, X. Wang, H. Wu and Z. Mu, *J. Lumin.*, 2013, **135**, 113-119.
- 23 P. F. Smet, J. Botterman, K. Van den Eeckhout, K. Korthout and D. Poelman, *Opt. Mater.*, 2014, **36**, 1913-1919.
- 24 Y. Zhuang, J. Ueda and S. Tanabe, *J. Mater. Chem. C*, 2013, **1**, 7849-7855.
- 25 Y. Zhuang, J. Ueda and S. Tanabe, *Appl. Phys. Express*, 2013, **6**, 052602.
- 26 A. Lecointre, A. Bessière, B. Viana and D. Gourier, *Radiat. Meas.*, 2010, **45**, 497-499.
- 27 L. Lin, C. Shi, Z. Wang, W. Zhang and M. Yin, *J. Alloy. Compd.*, 2008, **466**, 546-550.
- 28 A. Winterstein, H. Akamatsu, D. Möncke, K. Tanaka, M. Schmidt and L. Wondraczek, *Opt. Mater. Express*, 2013, **3**, 184-193.
- 29 I. Machado, L. Prado, L. Gomes, J. Prison and J. Martinelli, *J. Non-Cryst. Solids*, 2004, **348**, 113-117.
- 30 N. Da, M. Peng, S. Krolkowski and L. Wondraczek, *Opt. Express*, 2010, **18**, 2549-2557.
- 31 B. Padlyak, O. Vlokh, B. Kuklinski and K. Sagoo, *Ukr. J. Phys. Opt.*, 2006, **7**, 1-10.
- 32 C. Li, Q. Su and S. Wang, *Mater. Res. Bull.*, 2002, **37**, 1443-1449.
- 33 Y. Takahashi, M. Ando, R. Ihara and T. Fujiwara, *Opt. Mater. Express*, 2011, **1**, 372-378.
- 34 J. Qiu, H. Igarashi and A. Makishima, *Sci. Technol. Adv. Mater.*, 2005, **6**, 431-434.
- 35 Y. Zhuang, J. Ueda and S. Tanabe, *Appl. Phys. Lett.*, 2014, **105**, 191904.
- 36 S. Chenu, E. Véron, C. Genevois, G. Matzen, T. Cardinal, A. Etienne, D. Massiot and M. Allix, *Adv. Opt. Mater.*, 2014, **2**, 364-372.
- 37 S. Chenu, E. Véron, C. Genevois, A. Garcia, G. Matzen and M. Allix, *J. Mater. Chem. C*, 2014, **2**, 10002-10010.
- 38 G. Gao and L. Wondraczek, *J. Mater. Chem. C*, 2013, **1**, 1952-1958.
- 39 J. Pilbrow, *Transition ion electron paramagnetic resonance*, Clarendon Press Oxford, 1990.
- 40 A. Winterstein-Beckmann, D. Möncke, D. Palles, E. Kamitsos and L. Wondraczek, *J. Non-Cryst. Solids*, 2013, **376**, 165-174.
- 41 Z. Xia, Y. Zhang, M. S. Molokeev and V. V. Atuchin, *J. Phys. Chem. C*, 2013, **117**, 20847-20854.
- 42 K. Li, D. Geng, M. Shang, Y. Zhang, H. Lian and J. Lin, *J. Phys. Chem. C*, 2014, **110**, 11026-11034.
- 43 N. Guo, Y. Huang, Y. Jia, W. Lv, Q. Zhao, W. Lü, Z. Xia and H. You, *Dalton Trans.*, 2013, **42**, 941-947.

- 44 W. Lü, Z. Hao, X. Zhang, Y. Luo, X. Wang and J. Zhang, *Inorg. Chem.*, 2011, **50**, 7846-7851.
- 45 L. Van Uitert, *J. Electrochem. Soc.*, 1967, **114**, 1048-1053.
- 46 B. Padlyak and B. Kukliński, *Radiat. Meas.*, 2004, **38**, 593-597.
- 47 C. Shalgaonkar and A. Narlikar, *J. Mater. Sci.*, 1972, **7**, 1465-1471.
- 48 S. W. McKeever, *Thermoluminescence of solids*, Cambridge University Press, 1988.

Table and Figure captions

Table 1 Band-fitting parameters and estimated trap energy level E of glass sample G-Mn-0.1 and glass-ceramic samples GC-0.5h, GC-1h, GC-2h and GC-5h.

Fig. 1. Unit cell of $\text{NaAlGe}_3\text{O}_8$ drawn on basis of crystallographic data on ICSD# 61170.

Fig. 2. Electron paramagnetic resonance (EPR) spectra of glass sample G-Mn-0.1 and glass-ceramic samples GC-1h and GC-5h measured at 85 K.

Fig. 3. (a) Emission spectra ($\lambda_{\text{ex}} = 250 \text{ nm}$) of as-prepared glass samples G-Mn- x , the values of Mn content x are indicated; (b) Integrated emission intensities versus the Mn content x . Fitting to Eq. (1) is performed with $k=9.1\pm 1.0$, $\beta=1.8\pm 0.37$, and $\theta=6$, depicted as the solid black line; (c) Emission decay curve for glass samples G-Mn- x ($\lambda_{\text{ex}} = 250 \text{ nm}$, $\lambda_{\text{em}} = 645 \text{ nm}$), the inset shows the dependence of lifetime on the Mn content x . (d) Excitation spectra ($\lambda_{\text{em}} = 645 \text{ nm}$) of glass samples G-Mn- x , the inset shows the enlarged spectra in 400 to 550nm.

Fig. 4. Photographs of glass samples G-Mn-0.1 upon different crystallization time (0h~5h) and persistent time (0s~180s) after removal of excitation light of 254nm. Photos cannot be made for the longer persistent time because normal digital camera cannot recognize the weak signals.

Fig. 5. Afterglow spectra of the glass sample G-Mn-0.1. The samples were pre-irradiated with an UV-254nm lamp for 5 min and measured at different delay times (15 seconds to 48hours) after removing the lamp.

Fig. 6. TL curves of glass sample G-Mn-0.1 and glass-ceramic samples GC-0.5h, GC-1h, GC-2h and GC-5h as a function of temperature.

Fig. 7. (a) PL spectra ($\lambda_{\text{ex}} = 250 \text{ nm}$) and (b) Excitation spectra ($\lambda_{\text{em}} = 650 \text{ nm}$) of glass sample G-Mn-0.1 and glass-ceramic samples GC-0.5h, GC-1h, GC-2h and GC-5h. The curves were moved vertically for clarity. The inset of Fig. 7a shows the dependence of integrated PL intensity on crystallization time while the inset of Fig. 7b is the images of G-Mn-0.1, GC-0.5h, GC-1h, GC-2h and GC-5h.

Fig. 8. Afterglow decay curves of glass sample G-Mn-0.1 and glass-ceramic samples GC-0.5h, GC-1h, GC-2h and GC-5h.

Fig. 9. Afterglow spectra of the glass sample GC-5h. The samples were pre-irradiated with an UV-254nm lamp for 5 min and measured at different delay times (15 seconds to 104hours) after removing the lamp.

Fig. 10. XRD patterns of glass sample G-Mn-0.1 and glass-ceramic samples GC-0.5h, GC-1h, GC-2h and GC-5h. The simulated pattern of $\text{NaAlGe}_3\text{O}_8$ (ICSD #61170) is shown for reference at

the bottom of the figure.

Fig. 11. (a) High resolution TEM image of glass ceramic sample GC-5h, scale bar is 20 nm; Inset: the HR-TEM image of the sample, scale bar 2nm. Red circle denotes the boundary between glass and crystal phases. The distance between neighbored crystal lattice fringes is $\sim 0.328\text{nm}$, and it corresponds to the (002) crystal facet of albite $\text{Na}(\text{Al,Ga})\text{Ge}_3\text{O}_8$ solid solution compound. (b)-(f) Two-dimensional elemental mapping of the distribution of Na, Al, Ge, Ga, and O, respectively.

Fig. 12. Schematic of the mechanism of persistent luminescence processes in the Mn^{2+} doped glasses and glass-ceramics. EC1, EC2 and EC3 stand for the different types of octahedral Mn^{2+} emission centers; for clarity, only the ground state ${}^6\text{A}_1$ (${}^6\text{S}$) and the first excited state ${}^4\text{T}_1$ (${}^4\text{G}$) of Mn^{2+} are shown. D1, D2 and D3 stand for the different types of defects with depth as shown in Table 1. Dark red solid circles are electrons while white solid circles are holes. Paths 1 to 6 denote the different processes involved in the generation of the persistent luminescence processes.

Table 1 Band-fitting parameters and estimated trap energy level E of glass sample G-Mn-0.1 and glass-ceramic samples GC-0.5h, GC-1h, GC-2h and GC-5h.

Samples	Peak1	Trap1	Peak 2	Trap2	Peak 3	Trap3
	T_m (K)	E (eV)	T_m (K)	E (eV)	T_m (K)	E (eV)
G-Mn-0.1	354	0.71	401	0.80	529	1.06
GC-0.5h	348	0.70	376	0.75	416	0.83
GC-1h	349	0.70	374	0.775	417	0.83
GC-2h	347	0.69	372	0.74	417	0.83
GC-5h	348	0.70	376	0.75	423	0.85

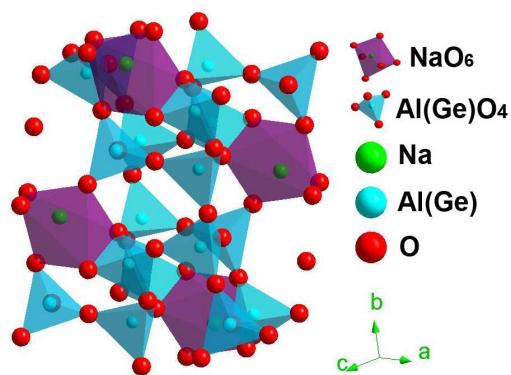


Fig. 1. Unit cell of $\text{NaAlGe}_3\text{O}_8$ drawn on basis of crystallographic data on ICSD# 61170.

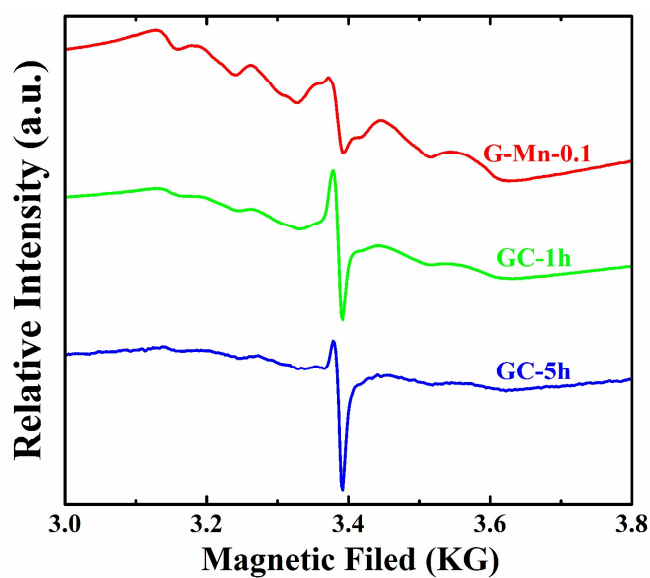


Fig. 2. Electron paramagnetic resonance (EPR) spectra of glass sample G-Mn-0.1 and glass-ceramic samples GC-1h and GC-5h measured at 85 K.

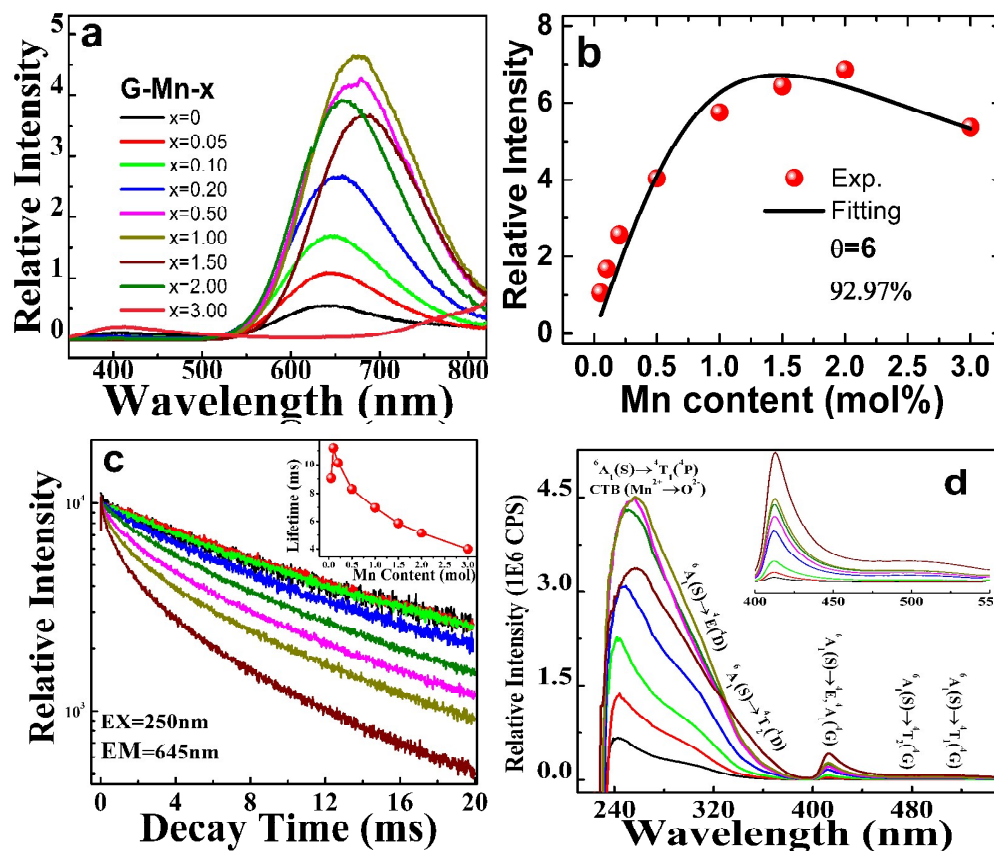


Fig. 3. (a) Emission spectra ($\lambda_{\text{ex}} = 250 \text{ nm}$) of as-prepared glass samples G-Mn-x, the values of Mn content x are indicated; (b) Integrated emission intensities versus the Mn content x . Fitting to Eq. (1) is performed with $k=9.1 \pm 1.0$, $\beta=1.8 \pm 0.37$, and $\theta=6$, depicted as the solid black line; (c) Emission decay curve for glass samples G-Mn-x ($\lambda_{\text{ex}} = 250 \text{ nm}$, $\lambda_{\text{em}} = 645 \text{ nm}$), the inset shows the dependence of lifetime on the Mn content x . (d) Excitation spectra ($\lambda_{\text{em}} = 645 \text{ nm}$) of glass samples G-Mn-x, the inset shows the enlarged spectra in 400 to 550 nm.

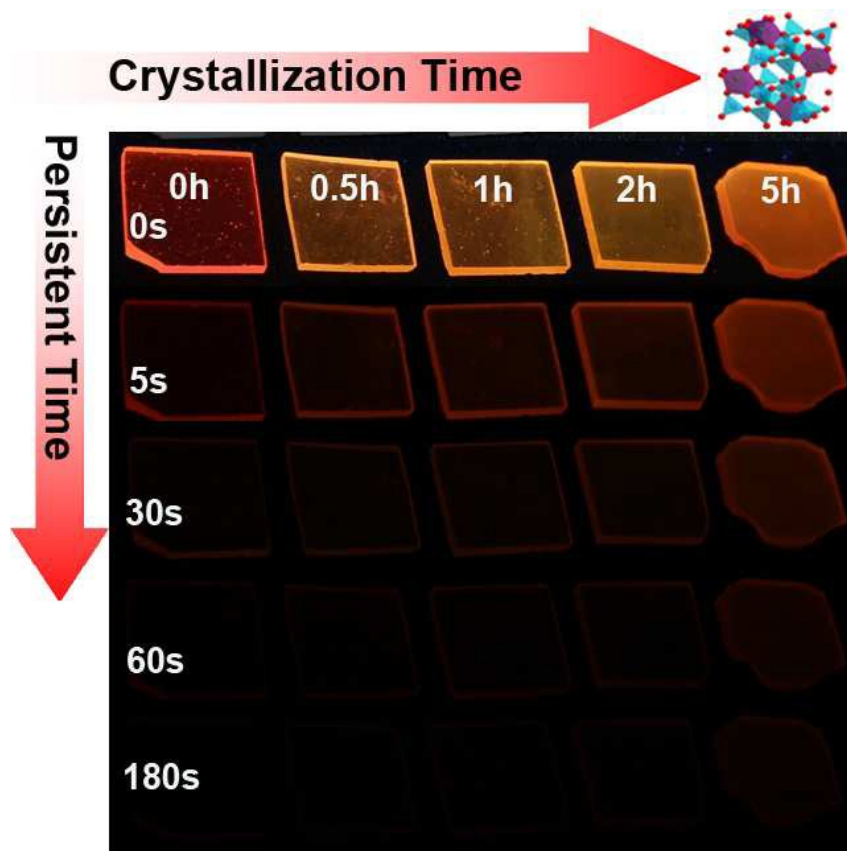


Fig. 4. Photographs of glass samples G-Mn-0.1 upon different crystallization time (0h~5h) and persistent time (0s~180s) after removal of excitation light of 254nm. Photos cannot be made for the longer persistent time because normal digital camera cannot recognize the weak signals.

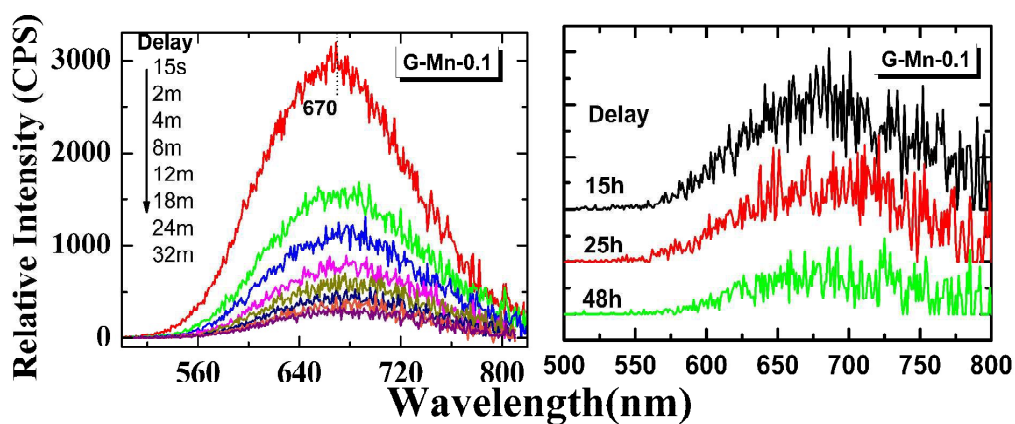


Fig. 5. Afterglow spectra of the glass sample G-Mn-0.1. The samples were pre-irradiated with an UV-254nm lamp for 5 min and measured at different delay times (15 seconds to 48hours) after removing the lamp.

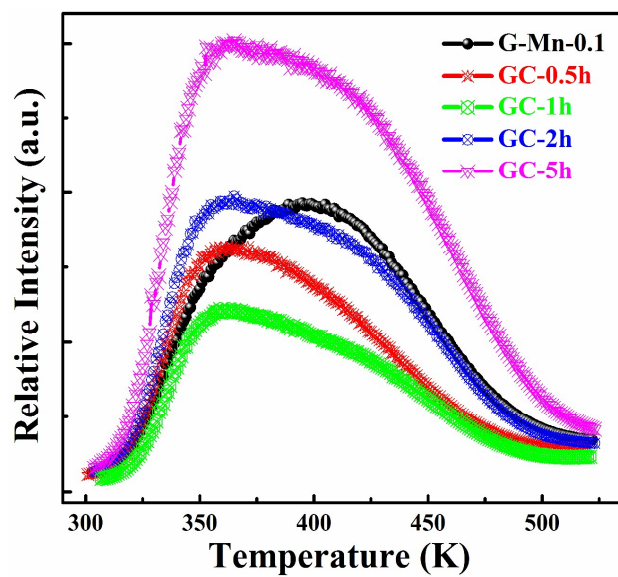


Fig. 6. TL curves of glass sample G-Mn-0.1 and glass-ceramic samples GC-0.5h, GC-1h, GC-2h and GC-5h as a function of temperature.

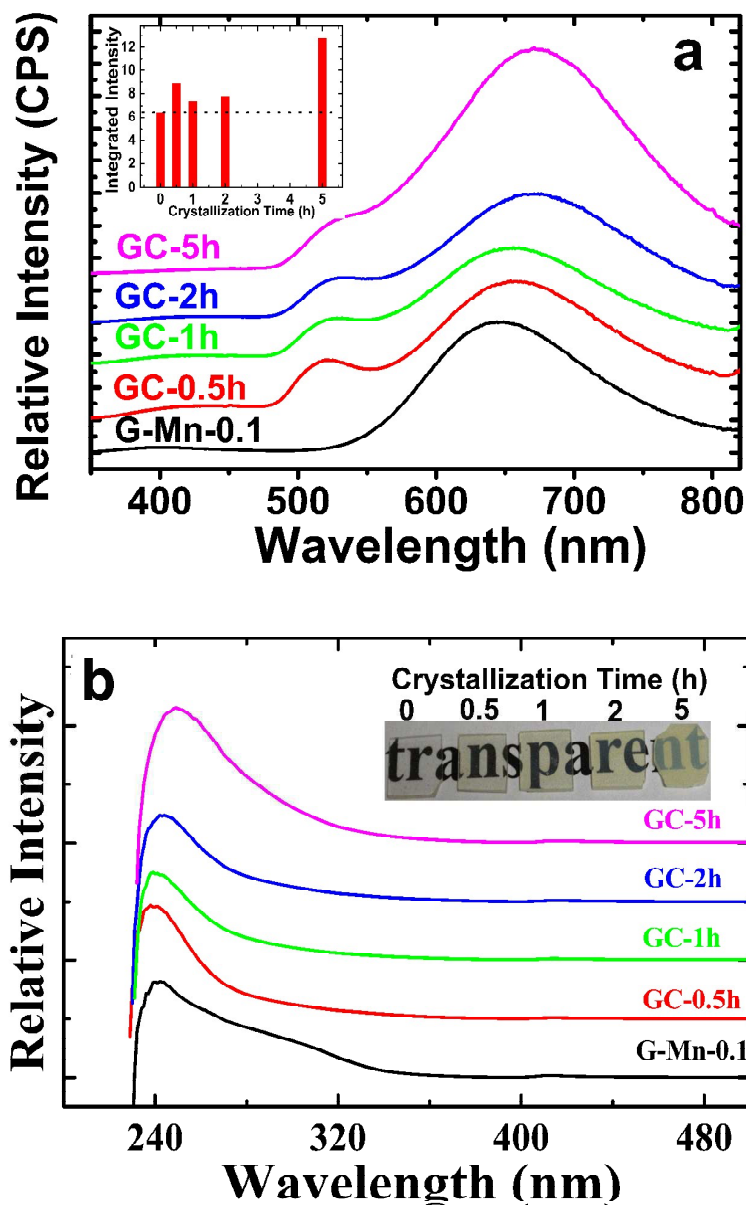


Fig. 7. (a) PL spectra ($\lambda_{\text{ex}} = 250$ nm) and (b) Excitation spectra ($\lambda_{\text{em}} = 650$ nm) of glass sample G-Mn-0.1 and glass-ceramic samples GC-0.5h, GC-1h, GC-2h and GC-5h. The curves were moved vertically for clarity. The inset of Fig. 7a shows the dependence of integrated PL intensity on crystallization time while the inset of Fig. 7b is the images of G-Mn-0.1, GC-0.5h, GC-1h, GC-2h and GC-5h.

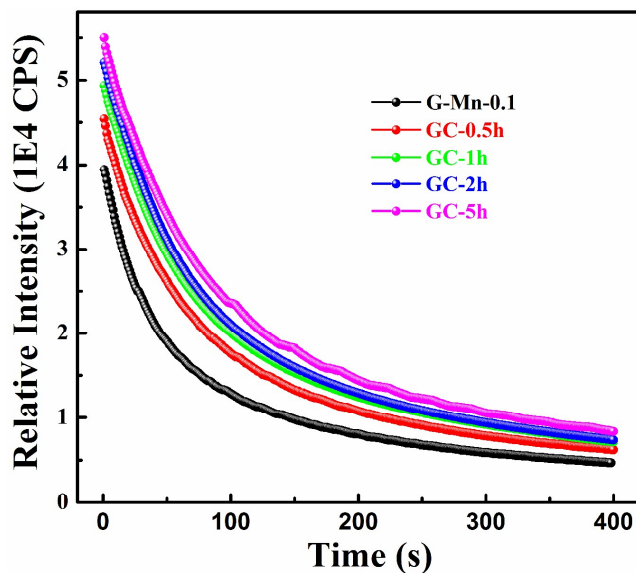


Fig. 8. Afterglow decay curves of glass sample G-Mn-0.1 and glass-ceramic samples GC-0.5h, GC-1h, GC-2h and GC-5h.

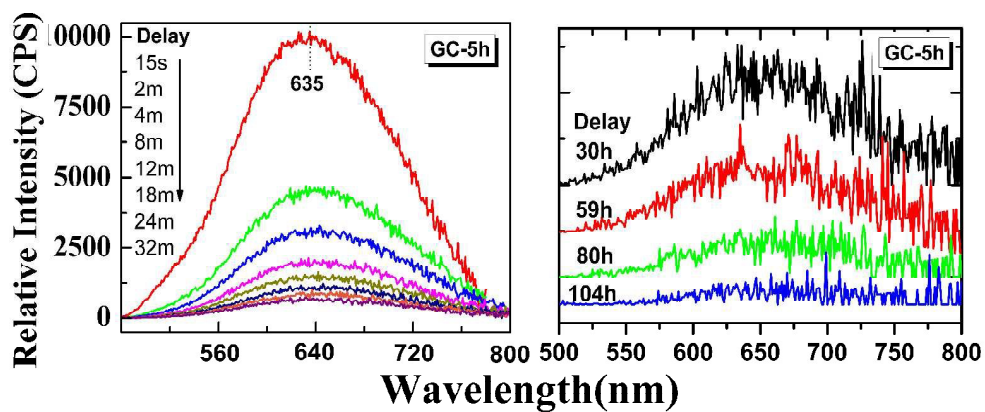


Fig. 9. Afterglow spectra of the glass sample GC-5h. The samples were pre-irradiated with an UV-254nm lamp for 5 min and measured at different delay times (15 seconds to 104hours) after removing the lamp.

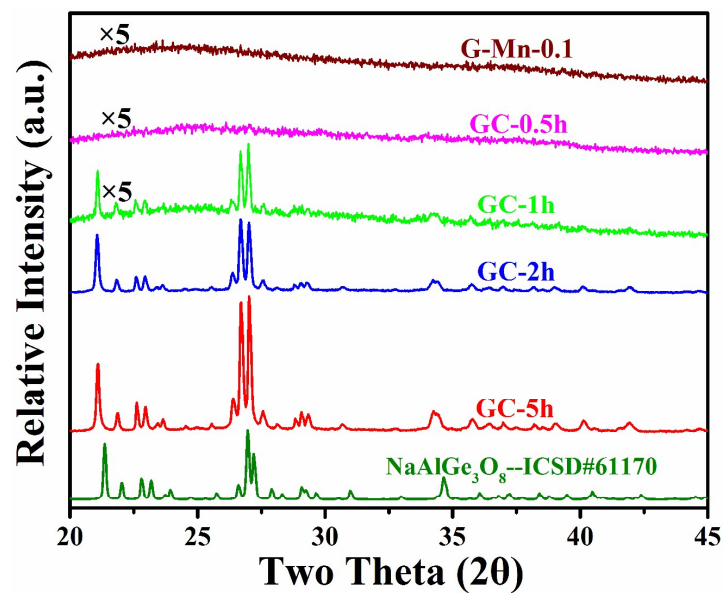


Fig. 10. XRD patterns of glass sample G-Mn-0.1 and glass-ceramic samples GC-0.5h, GC-1h, GC-2h and GC-5h. The simulated pattern of NaAlGe₃O₈ (ICSD #61170) is shown for reference at the bottom of the figure.

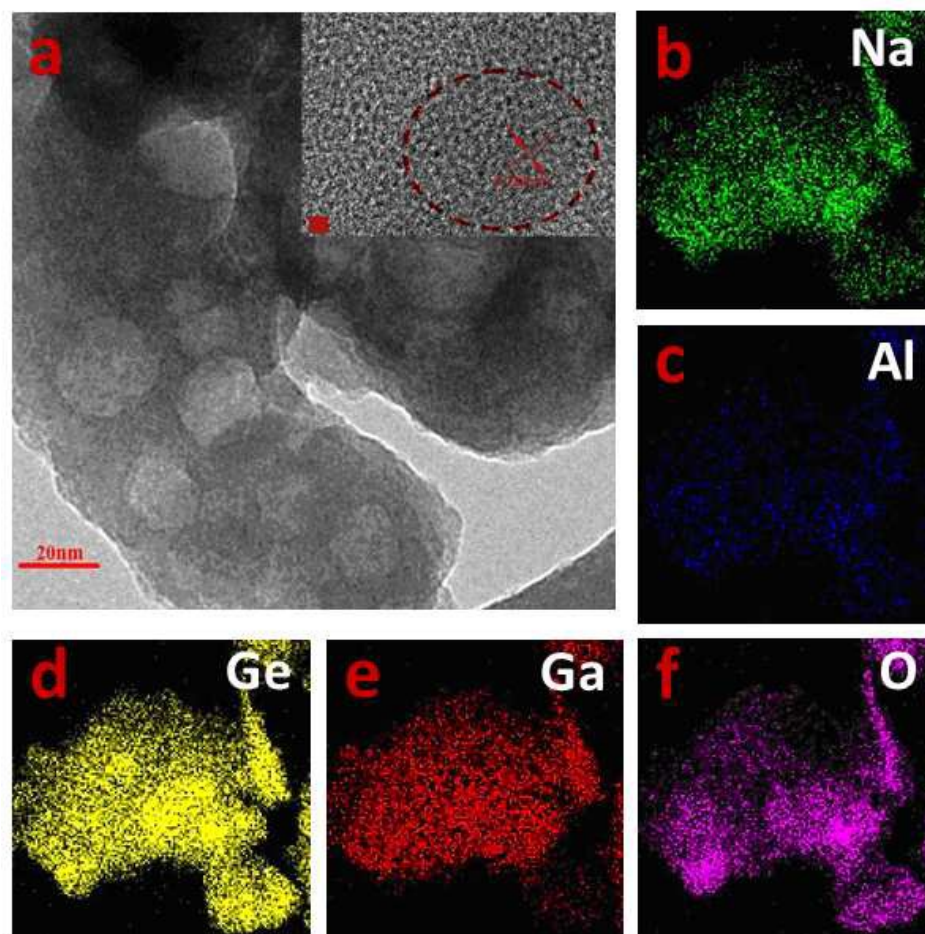


Fig. 11. (a) High resolution TEM image of glass ceramic sample GC-5h, scale bar is 20 nm; Inset: the HR-TEM image of the sample, scale bar 2nm. Red circle denotes the boundary between glass and crystal phases. The distance between neighbored crystal lattice fringes is ~ 0.328 nm, and it corresponds to the (002) crystal facet of albite $\text{Na}(\text{Al,Ga})\text{Ge}_3\text{O}_8$ solid solution compound. (b)-(f) Two-dimensional elemental mapping of the distribution of Na, Al, Ge, Ga, and O, respectively.

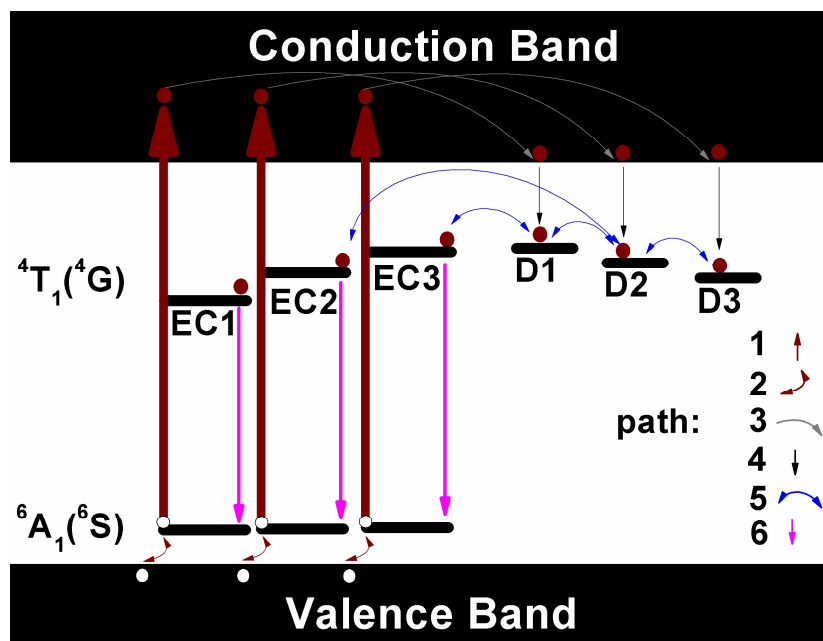
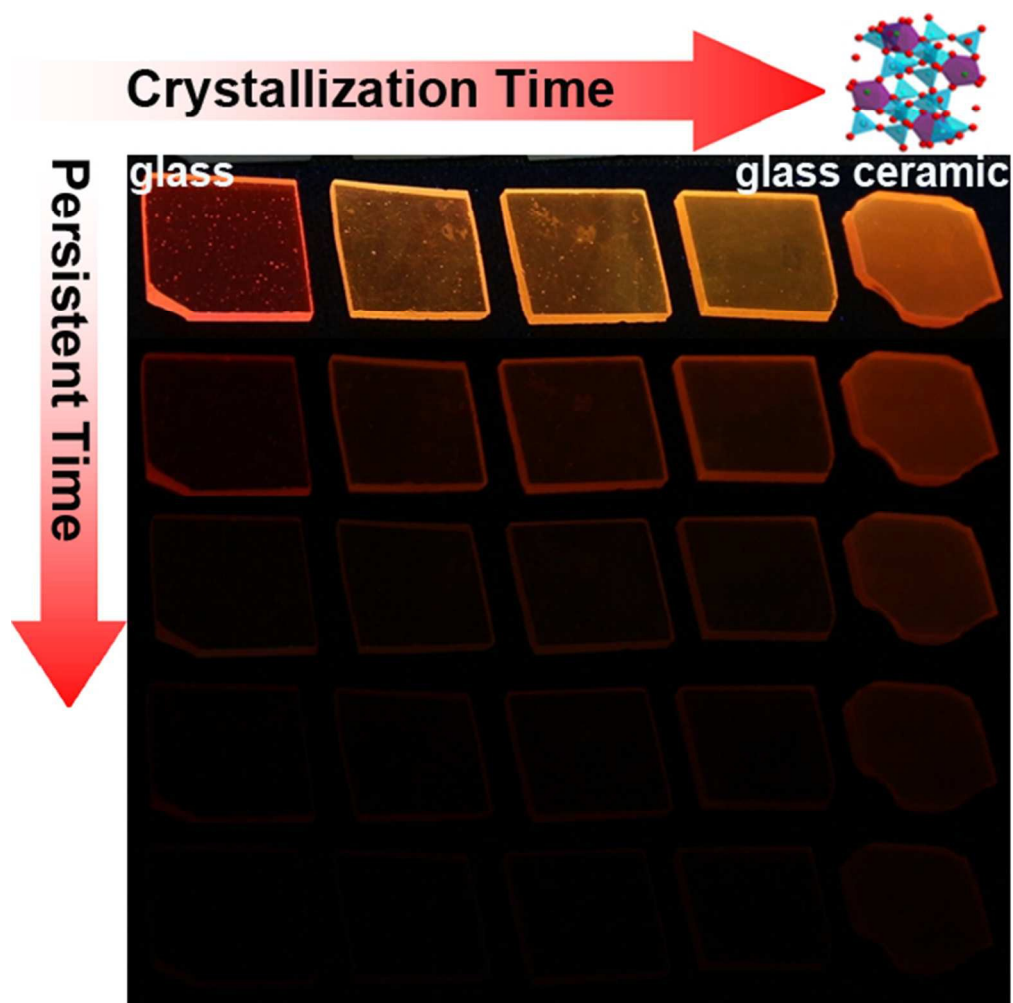


Fig. 12. Schematic of the mechanism of persistent luminescence processes in the Mn²⁺ doped glasses and glass-ceramics. EC1, EC2 and EC3 stand for the different types of octahedral Mn²⁺ emission centers; for clarity, only the ground state ${}^6A_1({}^6S)$ and the first excited state ${}^4T_1({}^4G)$ of Mn²⁺ are shown. D1, D2 and D3 stand for the different types of defects with depth as shown in Table 1. Dark red solid circles are electrons while white solid circles are holes. Paths 1 to 6 denote the different processes involved in the generation of the persistent luminescence processes.



Red to near infrared ultralong lasting luminescence from Mn²⁺-doped sodium gallium aluminum germanate glasses and (Al,Ga)-albite glass-ceramics
170x170mm (96 x 96 DPI)